2022-05-27

Water wave interactions with perforated elastic disks: Quadratic pressure discharge condition

Liang, H

Title:

Water wave interactions with perforated elastic disks: Quadratic pressure discharge condition

Journal:
Physical Review Fluids

Author names and affiliations:
Hui Liang[1], Siming Zheng[2,3*], Allan Magee[1], Deborah Greaves[2]

1 Technology Centre for Offshore and Marine, Singapore (TCOMS), 118411, Singapore
2 School of Engineering, Computing and Mathematics, University of Plymouth, Drake Circus, Plymouth PL4 8AA, United Kingdom
3 State Key Laboratory of Hydroscience and Engineering, Tsinghua University, Beijing, 100084, China
* Email address for correspondence: siming.zheng@plymouth.ac.uk

Water wave interactions with perforated elastic disks: Quadratic pressure discharge condition

Hui Liang[1], Siming Zheng[2,3,*], Allan Magee[1], Deborah Greaves[2]

1: Technology Centre for Offshore and Marine,

Singapore (TCOMS), 118411, Singapore

2: School of Engineering, Computing and Mathematics,

University of Plymouth, Drake Circus,

Plymouth PL4 8AA, United Kingdom and

3: State Key Laboratory of Hydroscience and Engineering,

Tsinghua University, Beijing, 100084, China

(Dated: June 4, 2022)

Abstract

A numerical model within the framework of the linear potential flow theory is developed to study interactions between water waves and perforated elastic disks. The boundary element method for hydrodynamic loads and modal function expansion for structural deformation are closely coupled, and disks are either simply supported or clamped at their edges. To model the flow past a perforated surface, a quadratic pressure drop model of practical validity is adopted. The established numerical model is applied to perform a multi-parameter study to investigate the effects of wave amplitude, flexural rigidity, edge conditions, and open-area ratio on the hydrodynamic responses. It is found that the nondimensional hydrodynamic responses, including: wave exciting force, hydroelastic deflection, and wave energy absorption, are increased with the increasing the incident wave amplitude due to the nonlinear nature of the quadratic pressure discharge model. With the increasing the flexural rigidity or rendering stronger constraints at the edge, the perforated elastic disk experiences an increase in the wave exciting force but a reduction in hydroelastic deflection, whereas they have negligible effects on the wave power absorption.

Keywords: Perforated disk; Hydroelasticity; Wave energy absorption; Boundary element method

I. INTRODUCTION

The study of interactions between water waves and impermeable/perforated rigid/flexible plates of small thickness is a fundamental problem, and thus has received considerable attention because of applications in motion reduction of a spar platform [1, 2], wave energy harnessing [3–6], wave absorber in wave flumes [7–9], and wave dissipation by submerged breakwaters [10–12], etc. In potential flow modelings, a perforated plate is usually regarded as a homogeneous surface, through which the flow is subject to a pressure drop condition. The pressure drop across a perforated surface can be either linearly or quadratically dependent on the normal velocity [13].

Due to its simple nature, a linear pressure drop condition based on the Darcy's law [14, 15] has been widely applied to model the damping effect of the flow past a perforated plate [3–6, 9, 16–18]. As pointed out by Taylor [19], however, the Darcy's law based linear pressure drop condition only applies to very tiny openings or fine-grained porous medium. Therefore, it is questionable to tackle a perforated surface with relatively large openings, where the flow separation becomes consequential, using the linear pressure discharge condition. Instead, studies suggest that the pressure drop across a perforated surface is relevant to the square of normal velocity component [20–23], according to the drag force term of the Morison equation. Moreover, experimental measurements [24–26] provide strong evidence that the hydrodynamic coefficients of perforated plates are dependent on the wave steepness or the motion amplitude, and this issue cannot be represented by a linear pressure drop model. Therefore, sufficient evidence in the fields of coastal and ocean engineering as reviewed in [13, 20] demonstrates the quadratic pressure discharge model is of practical validity. When the quadratic pressure discharge condition is imposed, another remarkable feature is that the hydrodynamic coefficients due to wave radiation are no longer symmetric [23].

When plate-shaped structures are used for submerged breakwaters and wave energy conversion, elastic deformation is non-negligible due to small thickness of plates [4, 5, 8, 11]. Unlike the conventional nearly rigid marine structures in which the hydrodynamic loads can be precalculated, there exhibits a strong dependency between hydrodynamic forces and elastic deformation of the structure. Therefore, the hydrodynamic loads must be determined together with the elastic deformations [27], which means a fully coupled model is required.

In the present study, water wave interactions with perforated elastic disks are considered via coupling the boundary element method for hydrodynamic loads and modal function expansion for structural deformation of the disk. Compared to the previous study [6] on water wave interactions

2

with perforated disks, two extensions have been made, including: (1) hydroelasticity of disks is considered; (2) a more practical quadratic pressure drop model is used instead of the linear one. To deal with the first issue, the structural deflection of each disk is expanded into modal functions, in which eigenvalues are determined by the edge boundary conditions, and then the modal function expansions for structural responses are fully coupled with the boundary element method for hydrodynamic loads. As for the second issue, the nonlinear nature of the quadratic pressure discharge condition gives rise to a nonlinear equation system, which will be solved by means of an iteration procedure.

The layout of the paper is as follows. Basic equations and assumptions are presented in Sec. II. In Sec. III, a numerical model coupling hydrodynamic loads and structural responses is established, and both linear and quadratic pressure drop models are considered. The method to determine hydrodynamic forces and wave power absorption is elucidated in Sec. IV. The verification of the developed numerical method is conducted in Sec. V via comparing the numerical solutions with the existing benchmark results documented in the literature. Section VI sets forth a multi-parameter study to investigate the influence of physical parameters on wave forces, wave energy harnessing, and hydroelastic responses. Finally, concluding remarks and future perspectives are presented in Sec. VII.

II. BASIC EQUATIONS

A three-dimensional Cartesian system of coordinates $Oxyz$ is defined with the Oxy plane coinciding with the undisturbed free surface and Oz axis orienting positively upward as illustrated in Fig. 1. Perforated elastic plates are submerged beneath a free surface under incident wave water actions. It is assumed that the fluid is inviscid and incompressible, and the flow is irrotational and time harmonic. Therefore, there exists a velocity potential $\Phi(\mathbf{x},t)$ satisfying the Laplace equation $\nabla^2\Phi = 0$ in a fluid domain of infinite lateral extent and water depth h, with $\mathbf{x} \equiv (x,y,z)$. In a steady state of time harmonic flows, the velocity potential $\Phi(\mathbf{x},t)$, velocity potential jump across the plate $\Psi(\mathbf{x},t) = \Phi^+(\mathbf{x},t) - \Phi^-(\mathbf{x},t)$, and the elastic deformation of plates $Z(\mathbf{x},t)$ are written as

$$\Phi(\mathbf{x},t) = \mathrm{Re}[\phi(\mathbf{x})\mathrm{e}^{-\mathrm{i}\omega t}], \quad \Psi(\mathbf{x},t) = \mathrm{Re}[\psi(\mathbf{x})\mathrm{e}^{-\mathrm{i}\omega t}], \quad \text{and} \quad Z(\mathbf{x},t) = \mathrm{Re}[\eta(\mathbf{x})\mathrm{e}^{-\mathrm{i}\omega t}], \quad (1)$$

where ω denotes the angular frequency of oscillation, and t is time.

For the wave scattering problem, the velocity potential in the fluid domain can be decomposed
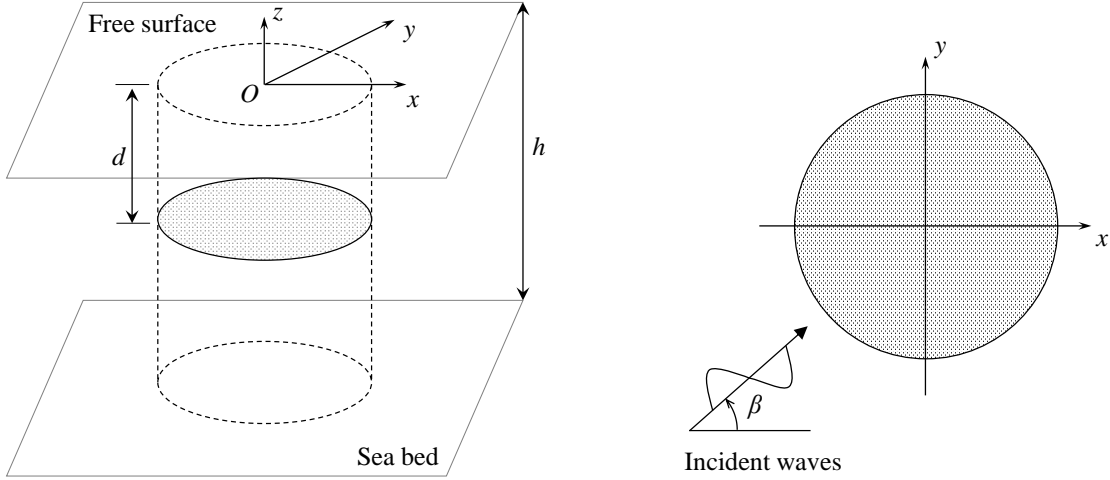
3

FIG. 1. Sketch of a submerged disk under wave actions and definition of coordinates.

into an incident wave potential $\phi_I(\mathbf{x})$, and a scattering potential $\phi_S(\mathbf{x})$, i.e., $\phi(\mathbf{x}) = \phi_I(\mathbf{x}) + \phi_S(\mathbf{x})$. Here, the incident wave potential $\phi_I(\mathbf{x})$ is written as [28]:

$$\phi_I(\mathbf{x}) = -\frac{igA}{\omega}\frac{\cosh[k_0(z+h)]}{\cosh k_0 h}e^{ik_0(x\cos\beta + y\sin\beta)}, \tag{2}$$

where β is the wave incidence angle as shown in Fig. 1, A the wave amplitude, g the acceleration due to gravity, and k_0 the wavenumber subjected to the dispersion relation $\omega^2 = gk_0\tanh(k_0h)$.

On the perforated elastic disk, the dynamic and kinematic conditions are satisfied. The dynamic condition is written as [5]

$$g\left(\chi\bar{\nabla}^4 - \frac{\omega^2}{g}\gamma\right)\eta + i\omega\psi = 0, \tag{3}$$

where $\bar{\nabla}$ represents the gradient with respect to variables on the disk's plane, $\chi = D/(\rho g)$ and $\gamma = \rho_D H/\rho$ denote the flexural rigidity and the mass per unit area, respectively, in which D is the flexural rigidity, ρ and ρ_D represent the water density and the density of the disk, respectively, and H is the thickness of the disk.

The kinematic condition is associated with the pressure jump across the plate, and both linear and quadratic pressure discharge conditions are considered herein. For the linear pressure drop condition, the kinematic body boundary condition is [3–5]

$$\frac{\partial\phi(\mathbf{x})}{\partial n} = -i\omega\eta(\mathbf{x}) - i\sigma(\mathbf{x})\psi(\mathbf{x}) = \frac{\partial\phi_S(\mathbf{x})}{\partial n} + \frac{\partial\phi_I(\mathbf{x})}{\partial n}, \quad \text{with } \sigma(\mathbf{x}) = \frac{k_0 b(\mathbf{x})}{2\pi}, \tag{4}$$

where n is the vector normal to the plate and defined positive upward, and $b(\mathbf{x})$ denotes the nondimensional linear perforation coefficient in the range $b \in [0, \infty)$ with $b = 0$ and $b = \infty$ corresponding to impermeable and transparent scenarios, respectively.

4

When the quadratic pressure drop condition [20]

$$P^+(\mathbf{x},t) - P^-(\mathbf{x},t) = -\frac{\rho}{2}\frac{1-\tau}{\mu\tau^2}\left|\frac{\partial\Phi(\mathbf{x},t)}{\partial n} - \frac{\partial Z(\mathbf{x},t)}{\partial t}\right|\left[\frac{\partial\Phi(\mathbf{x},t)}{\partial n} - \frac{\partial Z(\mathbf{x},t)}{\partial t}\right], \qquad (5)$$

is adopted, the application of the linearization method of equivalent work [29] gives rise to the kinematic body boundary condition for the quadratic pressure-velocity relation

$$\psi(\mathbf{x}) = \frac{4\mathrm{i}}{3\pi\omega}\frac{1-\tau}{\mu\tau^2}\left[\frac{\partial\phi_{\mathrm{I}}(\mathbf{x})}{\partial n} + \frac{\partial\phi_{\mathrm{S}}(\mathbf{x})}{\partial n} + \mathrm{i}\omega\eta(\mathbf{x})\right]\left\|\frac{\partial\phi_{\mathrm{I}}(\mathbf{x})}{\partial n} + \frac{\partial\phi_{\mathrm{S}}(\mathbf{x})}{\partial n} + \mathrm{i}\omega\eta(\mathbf{x})\right\|, \qquad (6)$$

where μ is the pressure loss coefficient ranging from 0.5 to 1.0, τ the open area ratio ranging from 0 to 1 with $\tau = 0$ and $\tau = 1$ corresponding to impermeable and transparent scenarios, respectively, and $\|\cdot\|$ the module of a complex number.

III. NUMERICAL MODEL

The Laplace equation will be solved by a boundary element method (BEM). Following [30, 31], a disk of vanishing thickness is represented by a dipole distribution, and the scattering potential is then expressed as:

$$\phi_{\mathrm{S}}(\mathbf{x}) = -\frac{1}{4\pi}\iint_S \psi(\mathbf{x}_0)\frac{\partial G(\mathbf{x},\mathbf{x}_0)}{\partial n_{\mathbf{x}_0}}\mathrm{d}S, \qquad (7)$$

where $\mathbf{x}_0 \equiv (x_0, y_0, z_0)$ and $\mathbf{x} \equiv (x, y, z)$ stand for the singularity point and flow-field point, respectively, S denotes the disk surface, and $G(\mathbf{x}, \mathbf{x}_0)$ is the free-surface Green function in a finite water depth h given by [32]

$$\begin{aligned}
G(\mathbf{x},\mathbf{x}_0) = &-\frac{1}{\sqrt{\mathscr{R}^2 + (z-z_0)^2}} - \frac{1}{\sqrt{\mathscr{R}^2 + (z+z_0+2h)^2}}\\
&-2\int_0^\infty \frac{(\kappa+K)\cosh\kappa(z+h)\cosh\kappa(z_0+h)}{\kappa\sinh\kappa h - K\cosh\kappa h}\mathrm{e}^{-\kappa h}J_0(\kappa\mathscr{R})\mathrm{d}\kappa,
\end{aligned} \qquad (8)$$

where $K = \omega^2/g$ denotes the wavenumber in deep water, $\mathscr{R} = \sqrt{(x-x_0)^2 + (y-y_0)^2}$ is the horizontal distance between the singularity point and flow-field point, and $J_0(u)$ is zeroth-order Bessel function of the first kind [33]. The Green function $G(\mathbf{x}, \mathbf{x}_0)$ given by Eq. (8) satisfies the Laplace equation, linear free-surface boundary condition, seabed condition, and radiation condition in the far field.

To determine the distribution of velocity potential jump $\psi(\mathbf{x}_0)$, the body boundary condition is enforced on the plate, and we obtain a hypersingular integral equation [6]

$$-\frac{1}{4\pi}\iint_S \psi(\mathbf{x}_0)\frac{\partial^2 G(\mathbf{x},\mathbf{x}_0)}{\partial n_{\mathbf{x}}\partial n_{\mathbf{x}_0}}\mathrm{d}S = \frac{\partial\phi_{\mathrm{S}}(\mathbf{x})}{\partial n}. \qquad (9)$$

5

In the numerical implementation, the disk is discretized into panels with constant strength. Capabilities of numerically solving hypersingular integral equations for wave effects on perforated structures have been demonstrated in [6, 34].

To account for the hydroelastic deflection, the edge conditions are required. In the present study, both clamped edge and simply supported edge conditions are considered. For the clamped edge, the vanishing of deflection and its radial derivative at the edge is imposed

$$
\begin{cases}
\eta(r,\theta) = 0 \\
\dfrac{\partial \eta(r,\theta)}{\partial r} = 0
\end{cases}
\quad \text{at} \quad r = R,
\tag{10}
$$

where R is the radius of the disk, and polar coordinates r and θ are defined as the distance to the center of the disk and the polar angle, respectively. For the simply supported edge, the deflection and bending moment at the edge are null

$$
\begin{cases}
\eta(r,\theta) = 0 \\
\dfrac{\partial^2 \eta(r,\theta)}{\partial r^2} + \dfrac{v}{R^2}\dfrac{\partial^2 \eta(r,\theta)}{\partial \theta^2} + \dfrac{v}{R}\dfrac{\partial \eta(r,\theta)}{\partial r} = 0
\end{cases}
\quad \text{at} \quad r = R,
\tag{11}
$$

where v denotes Poisson's ratio. Then, we expand the deformation of a circular plate into a Fourier-Bessel series

$$
\eta(r,\theta) = \sum_{k=-\infty}^{\infty} \sum_{l=0}^{\infty} \left[a_{k,l} J_k\left(\mu_{k,l}\frac{r}{R}\right) + b_{k,l} I_k\left(\mu_{k,l}\frac{r}{R}\right) \right] \mathrm{e}^{\mathrm{i}k\theta},
\tag{12}
$$

where $\mu_{k,l}$ denote the eigenvalues determined by edge conditions in Eq. (10) for clamped edge or Eq. (11) for simply supported edge, and $I_k(u)$ is the kth-order modified Bessel function of the first kind [33]. For the clamped edge and simply supported edge conditions considered here, the deflection at the edge is null, and Eq. (12) becomes

$$
\eta(r,\theta) = \sum_{k=-\infty}^{\infty} \sum_{l=0}^{\infty} a_{k,l} F_{k,l}(r) \mathrm{e}^{\mathrm{i}k\theta},
\tag{13}
$$

where the radial base function is written as

$$
F_{k,l}(r) = J_k\left(\mu_{k,l}\frac{r}{R}\right) - \frac{J_k(\mu_{k,l})}{I_k(\mu_{k,l})} I_k\left(\mu_{k,l}\frac{r}{R}\right).
\tag{14}
$$

A.   Linear pressure drop condition

Numerical implementation of the linear pressure drop condition is now considered. By applying the linear pressure drop condition in Eq. (4), the boundary integral equation is written as

$$
\mathrm{i}\sigma(\mathbf{x})\psi(\mathbf{x}) - \frac{1}{4\pi} \iint_S \psi(\mathbf{x}_0) \frac{\partial^2 G(\mathbf{x},\mathbf{x}_0)}{\partial n_{\mathbf{x}} \partial n_{\mathbf{x}_0}} \mathrm{d}S + \mathrm{i}\omega \sum_{k=-\infty}^{\infty} \sum_{l=0}^{\infty} a_{k,l} F_{k,l}(r) \mathrm{e}^{\mathrm{i}k\theta} = -\mathbf{n}\cdot\nabla\phi_{\mathrm{I}}(\mathbf{x})
\tag{15}
$$

6

The dynamic boundary condition on the disk given by Eq. (3) is enforced in a Galerkin manner via multiplying a test function

$$g_{m,n}(r,\theta) = F_{m,n}(r)e^{-im\theta} \tag{16}$$

and integrating the test function over the plate area giving rise to

$$i\omega \iint_S \psi(\mathbf{x})g_{m,n}(r,\theta)dS + g\sum_{k=-\infty}^{\infty}\sum_{l=0}^{\infty} a_{k,l}\left(\chi\frac{\mu_{k,l}^4}{R^4} - \frac{\omega^2}{g}\gamma\right)\mathscr{I}_{mn,kl} = 0, \tag{17}$$

where $\mathscr{I}_{mn,kl}$ is defined as

$$\mathscr{I}_{mn,kl} = 2\pi\delta_{m,k}\int_0^R rF_{m,n}(r)F_{k,l}(r)dr. \tag{18}$$

A combination of the hypersingular integral equation (15) and dynamic condition (17) gives rise to a linear equation system with unknowns ψ and $a_{k,l}$, which can be solved numerically. It is noted that Eqs. (15) and (17) are interconnected, and hydrodynamic forces and body's deformation influence each other. Therefore, the hydrodynamic loads and structural deflection are closely coupled.

B. Quadratic pressure drop condition

As a sequel to Sec. III A, the numerical implementation for the quadratic pressure discharge condition is now considered. Substituting the quadratic pressure drop condition in Eq. (6) into the hypersingular integral equation (9) yields

$$C(\mathbf{x})\psi(\mathbf{x}) - \frac{1}{4\pi}\iint_S \psi(\mathbf{x}_0)\frac{\partial^2 G(\mathbf{x},\mathbf{x}_0)}{\partial n_\mathbf{x}\partial n_{\mathbf{x}_0}}dS + i\omega\sum_{k=-\infty}^{\infty}\sum_{l=0}^{\infty}a_{k,l}F_{k,l}(r)e^{ik\theta} = -\mathbf{n}\cdot\nabla\phi_I(\mathbf{x}). \tag{19}$$

where $C(\mathbf{x})$ is defined as

$$C(\mathbf{x}) = \frac{3\pi i\omega\mu\tau^2}{4(1-\tau)}\left\|\frac{\partial\phi_I(\mathbf{x})}{\partial n} + \frac{\partial\phi_S(\mathbf{x})}{\partial n} + i\omega\sum_{k=-\infty}^{\infty}\sum_{l=0}^{\infty}a_{k,l}F_{k,l}(r)e^{ik\theta}\right\|^{-1}. \tag{20}$$

The dynamic condition is the same as Eq. (17). When the quadratic pressure drop condition is implemented, the hypersingular integral equation becomes nonlinear because the coefficient $C(\mathbf{x})$ is dependent on the scattering potential $\phi_S(\mathbf{x})$ and coefficients of Fourier-Bessel series $a_{k,l}$. Therefore, an iteration procedure is required to solve the nonlinear equation system as in [23], and the flow chart is illustrated in Fig. 2.
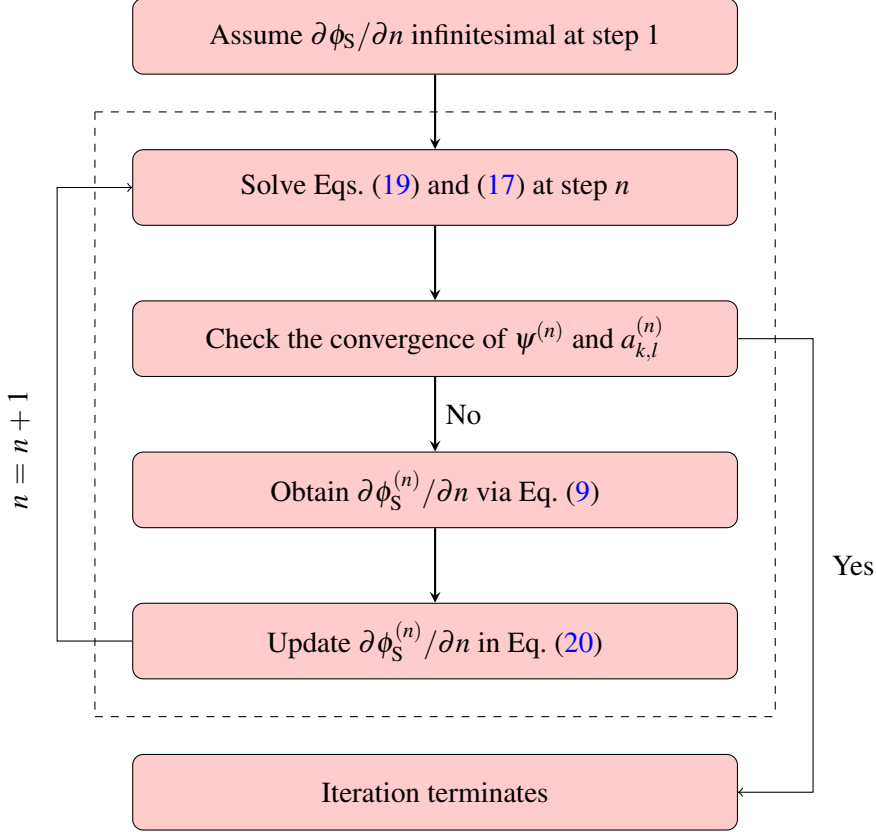
Assume $\partial\phi_S/\partial n$ infinitesimal at step 1

Solve Eqs. (19) and (17) at step n

Check the convergence of $\psi^{(n)}$ and $a_{k,l}^{(n)}$

No

Obtain $\partial\phi_S^{(n)}/\partial n$ via Eq. (9)

Update $\partial\phi_S^{(n)}/\partial n$ in Eq. (20)

$n = n + 1$

Yes

Iteration terminates

FIG. 2. Flow chart of the iteration procedure for solving a nonlinear equation system composed of Eqs. (19) and (17).

IV. HYDRODYNAMIC FORCES AND ENERGY ABSORPTION

Given the velocity jump across the disk ψ determined by the procedure elucidated in Sec. III, the wave exciting force on the disk can be obtained

$$\mathbf{F} = -\mathrm{i}\omega\rho \iint_S \psi(\mathbf{x})\mathbf{n}\mathrm{d}S. \tag{21}$$

Due to the fact that perforated plates can be used as a wave power take-off device, the wave energy absorption is now considered. According to Linton and McIver [35], the dissipated energy is defined as

$$E_{\mathrm{diss}} = -\rho \iint_S \overline{\frac{\partial\Psi(\mathbf{x},t)}{\partial t}\left[\frac{\partial\Phi(\mathbf{x},t)}{\partial n} - \frac{\partial Z(\mathbf{x},t)}{\partial t}\right]}\mathrm{d}S \tag{22}$$

where the overline denotes time average. Then, the time-averaged wave power absorbed by the disk is written as

$$E_{\mathrm{diss}} = -\frac{\rho\omega}{2}\iint_S \mathrm{Re}\left\{-\mathrm{i}\psi(\mathbf{x})\left[\frac{\partial\phi^*(\mathbf{x})}{\partial n} + \mathrm{i}\omega\eta^*(\mathbf{x})\right]\right\}\mathrm{d}S \tag{23}$$

8

where the asterisk denotes complex conjugate.

For the linear pressure drop condition given by Eq. (4), the corresponding energy absorption by a perforated plate is

$$E_{\text{diss}}^L = \frac{\rho \omega}{2} \iint_S \sigma(\mathbf{x}) \|\psi(\mathbf{x})\|^2 \mathrm{d}S, \tag{24}$$

which is consistent with the formulation in [3–5].

When the quadratic pressure drop condition is adopted, the representation of the energy absorption is

$$E_{\text{diss}}^Q = \frac{3\pi \rho \omega^2}{8} \frac{\mu \tau^2}{1-\tau} \iint_S \|\psi(\mathbf{x})\|^2 \left\| \frac{\partial \phi(\mathbf{x})}{\partial n} + i\omega \eta(\mathbf{x}) \right\|^{-1} \mathrm{d}S. \tag{25}$$

Given the incident wave energy per unit width [28]

$$E_{\text{in}} = \frac{\rho g A^2}{2} \frac{\omega}{2k_0} \left(1 + \frac{2k_0 h}{\sinh 2k_0 h} \right), \tag{26}$$

the nondimensional absorbed wave energy is written as

$$\kappa^{L,Q} = k_0 E_{\text{diss}}^{L,Q} / E_{\text{in}}, \tag{27}$$

where superscripts "L" and "Q" correspond to linear and quadratic pressure drop conditions, respectively.

V. VERIFICATION OF THE NUMERICAL MODEL

For verification purposes, hydrodynamic performances of perforated elastic disks subjected to the linear pressure drop condition and a perforated rigid disk under a quadratic pressure drop condition are considered. Comparison will be made with the results documented in the literature. In the subsequent numerical examples, each disk is discretized into 4,633 quadrilateral panels, and the Fourier-Bessel expansions in Eq. (13) are truncated by $k \in [-40, 40]$ and $l \in [0, 20]$. Convergence test has been conducted to confirm the convergence of the present setup.

A. Wave power absorption by a perforated elastic disk

Wave power harnessed by a perforated elastic disk subjected to the linear pressure discharge condition given by Eq. (4) is first considered. Figure 3 depicts the frequency responses of the nondimensional wave energy absorption κ^L defined in Eq. (27) at $R/h = 2.0$, $d/h = 0.2$, $\chi/h^4 =$

9
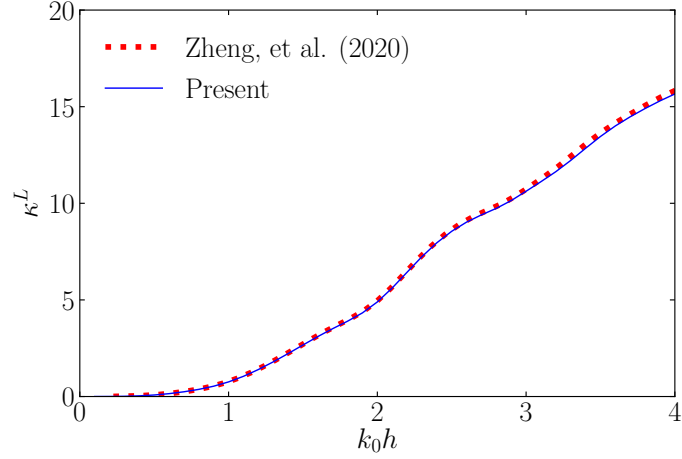
(a) Simply supported edge
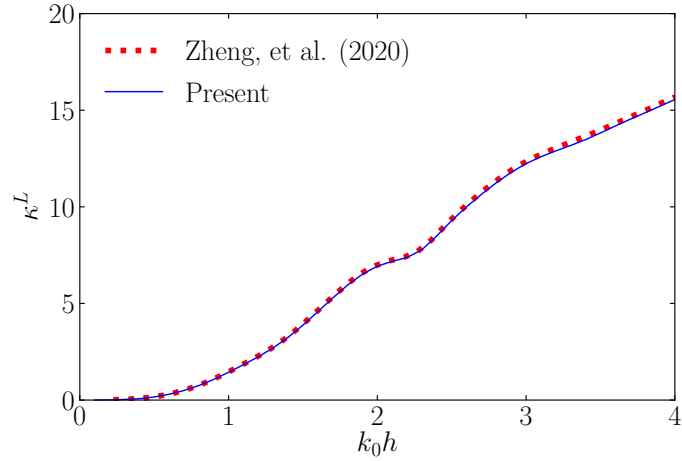
(b) Clamped edge

FIG. 3. Nondimensional wave power absorption κ^L as a function of normalized wavenumber $k_0 h$ at $R/h = 2.0$, $d/h = 0.2$, $\chi/h^4 = 0.01$, $\gamma/h = 0.01$, $\sigma h = 1.0$, and $\nu = 0.3$. Comparison is made with the analytical solutions by Zheng, et al. [4].

0.01, $\gamma/h = 0.01$, $\sigma h = 1.0$, and $\nu = 0.3$, where d denotes the submergence of the disk. Both simply supported and clamped edge conditions are considered as in subplots (a) and (b), respectively. Comparison is made with the results determined by the eigenfunction matching method by Zheng, et al. [4], and the agreement is satisfactory as expected.

B. Hydroelastic deflection of two side-by-side disks

Then, we consider the hydroelastic deformations of two identical perforated elastic disks in a side-by-side configuration at $k_0 h = \pi/2$, $R/h = 2.0$, $d/h = 0.2$, $\chi/h^4 = 0.01$, $\gamma/h = 0.01$, $\sigma h = 1.0$, and $\nu = 0.3$. Figure 4 illustrates the modulus of normalized hydroelastic deflections of the perforated elastic disks $\|\eta\|/A$, which are simply supported, and are subjected to the linear pressure drop condition. The center-to-center distance between the disks is $l/h = 5.0$, and the wave incidence angle is $\beta = 45°$. The results determined by the present numerical model and the analytical solutions by Zheng, et al. [4] are presented in subplots (a) and (b), respectively. There is visibly perfect agreement with the analytical solution, which demonstrates that the present numerical model is able to tackle the perforated elastic disks subjected to linear pressure discharge condition well.

C. A perforated rigid disk in heaving motion

As a sequel to the verification associated with the linear pressure drop condition, cases relevant to the quadratic pressure-velocity condition are now considered. Here, we are concerned with the added mass and damping by a perforated rigid disk undergoing time-harmonic heaving motion underneath a free surface as in [36], and the quadratic pressure-velocity condition given by Eq. (6) is used. For the wave radiation problem by a heaving rigid disk, the quadratic pressure discharge condition becomes

$$\psi(\mathbf{x}) = \frac{4\mathrm{i}}{3\pi\omega} \frac{1-\tau}{\mu\tau^2} \left[\frac{\partial\phi(\mathbf{x})}{\partial n} - \omega a \right] \left\| \frac{\partial\phi(\mathbf{x})}{\partial n} - \omega a \right\|, \tag{28}$$

where a is the amplitude of the heaving motion. By substituting Eq. (28) into the hypersingular integral equation (9), we can obtain the velocity potential jump ψ due to the heaving motion via solving a nonlinear equation system. Then, the added mass and damping due to heaving motion are determined

$$A_{33} = -\frac{\rho}{\omega a}\mathrm{Re}\iint_S \psi(\mathbf{x})\mathrm{d}S, \quad \text{and} \quad B_{33} = \mathrm{Re}\left[\frac{\mathrm{i}\rho}{a}\iint_S \psi(\mathbf{x})\mathrm{d}S \right]. \tag{29}$$

Figure 5 depicts the nondimensional added mass and damping coefficients by a heaving disk at an oscillatory period $T = 1.2$ s varying with the porous Keulegan-Carpenter number defined as

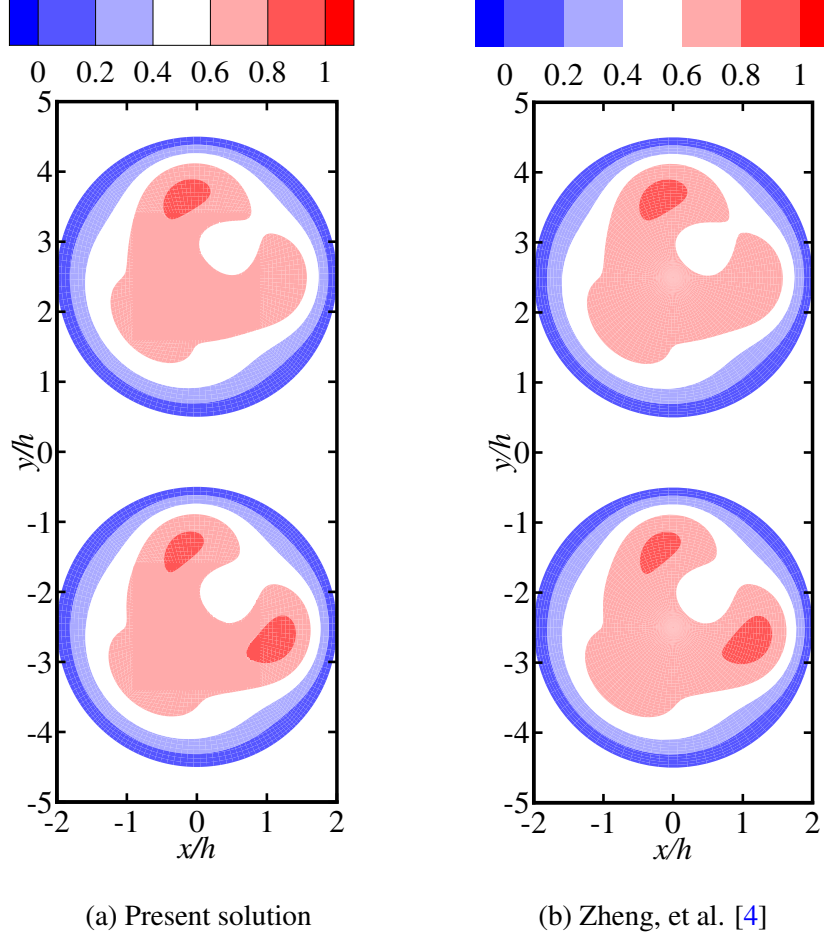$$K_C = \frac{1-\tau}{2\mu\tau^2}\frac{a}{R}. \tag{30}$$

11

FIG. 4. Modulus of normalized hydroelastic deflections of two perforated elastic disks $\|\eta\|/A$ in a side-by-side configuration subjected to a linear pressure discharge condition under a simply supported condition at $k_0 h = \pi/2$, $R/h = 2.0$, $d/h = 0.2$, $\chi/h^4 = 0.01$, $\gamma/h = 0.01$, $\sigma h = 1.0$, $\nu = 0.3$, and $\beta = 45°$. The present numerical results as in subplot (a) are compared with the analytical solutions by Zheng, et al. [4] displayed in subplot (b).

Using the same case as presented by Molin [36], the normalized radius of the disk is $R/h = 0.6$, and the submergence is $d/h = 0.5$. The pressure discharge coefficient is $\mu = 0.5$, and the open area ratio is $\tau = 0.2$. The heaving added mass and damping are nondimensionalized with respect to ρR^3, and $\omega \rho R^3$, respectively. Both added mass and damping are dependent on the motion amplitude due to the nonlinearity in the pressure discharge condition. Comparison is made with the analytical solutions by Molin [36], and generally good agreement has been obtained. This provides strong evidence that the present model is capable of dealing with the quadratic pressure drop condition as well.
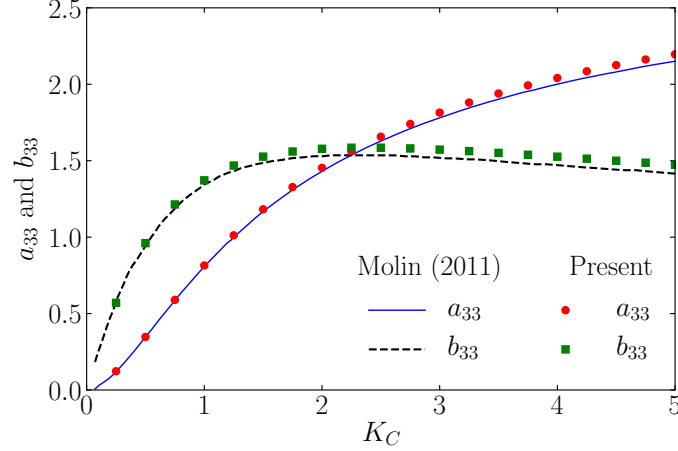
FIG. 5. Nondimensional added mass a_{33} and damping b_{33} of a heaving perforated rigid disk subjected to the quadratic pressure discharge condition versus the porous KC number at $\mu = 0.5$, $\tau = 0.2$, $R/h = 0.6$, $d/h = 0.5$, and $T = 1.2$ s. Comparison is made with the analytical solutions by Molin [20].

VI. NUMERICAL RESULTS AND DISCUSSIONS

Due to the fact that the hydrodynamic characteristics of perforated elastic disks subjected to the linear pressure discharge condition have been extensively studied in the existing literature [3–6], they will not be elucidated here. The focus is then placed on perforated elastic disks subjected to the quadratic pressure discharge condition in this section, and a multi-parameter analysis will be made to investigate the hydrodynamic responses, including: wave exciting force, hydroelastic deflection, and wave energy extraction.

A. Effect of incident wave amplitude

Figure 6 depicts the frequency responses of vertical wave exciting forces F_z and extracted wave energy κ^Q by a horizontal perforated flexible disk for different incident wave amplitudes, including: $A/h = 0.01$ and $A/h = 0.02$, at $R/h = 2.0$, $d/h = 0.2$, $\chi/h^4 = 0.01$, $\gamma/h = 0.01$, $\tau = 0.2$, $\mu = 0.5$, and $\nu = 0.3$. The wave exciting forces are normalized with respect to $\pi \rho g R^2 A$, and both simply supported edge and clamped edge conditions are considered. Due to the nonlinear characteristics of the quadratic pressure discharge condition, both wave exciting force and wave power absorption, shown in subplots (a) and (b), are dependent on the wave amplitude, and thus exhibit nonlinear correlations. Specifically, the higher the wave amplitude is, the larger wave ex-

13

citing force and harnessed wave energy are. Moreover, the disk subjected to the clamped edge condition experiences larger wave forces than that to the simply supported edge condition due to the stronger constraints at the clamped edge, especially in the range of long waves ($k_0h < 3.0$). However, the wave power absorbed by disks under two edge conditions are comparable except a frequency range $k_0h < 3.0$ where a disk subjected to the clamped edge harnesses slightly higher wave energy than that to the simply supported edge. At $A/h = 0.01$, the nondimensional wave energy absorption reaches a maximum at $k_0h \approx 6.3$, whereas the nondimensional wavenumber for maximum absorption at $A/h = 0.02$ shifts to $k_0h \approx 7.0$. Therefore, the frequency, at which the maximum wave power is absorbed, is dependent on the incident wave amplitude as well. It should be noted that, with the increasing the wave steepness, the nonlinearity of water waves becomes increasingly important, and therefore a high-order model would be desired to cope with this scenario.

### B. Effect of flexural rigidity

The influence of the flexural rigidity, including: $\chi/h^4 = 0.01$, $\chi/h^4 = 0.02$ and $\chi/h^4 = 0.04$, on the frequency responses of wave exciting forces F_z and absorbed wave energy κ^Q is presented in Fig. 7 at an incident wave amplitude $A/h = 0.02$, and other physical parameters are the same as in Fig. 6. With the increasing flexural rigidity, the disk experiences a larger wave exciting force as in subplot (a). However, in the computed range of wave frequencies, especially for $k_0h > 3.0$ as in subplot (a), the influence of the flexural rigidity on the wave power absorption is inconsequential because the extracted wave energy for different flexural rigidity parameters is comparable.

C. Effect of open-area ratio

Figure 8 exhibits the contour plot of nondimensional wave energy absorption κ^Q by a perforated flexible disk with the edge simply supported varying with the nondimensional wavenumber k_0h and open-area ratio τ at $R/h = 2.0$, $d/h = 0.2$, $\gamma/h = 0.01$, $\mu = 0.5$ and $\nu = 0.3$. The results for incident wave amplitudes $A/h = 0.01$ and $A/h = 0.02$ are displayed in subplots (a) and (b), respectively. When $\tau = 0$ and 1, which correspond to impermeable and transparent scenarios, respectively, no wave energy is harnessed as expected. In the range $\tau \in (0, 1)$, one can obtain an optimal open-area ratio $\tau = 0.08$ at which the largest wave power is extracted. When $\tau = 0.08$,
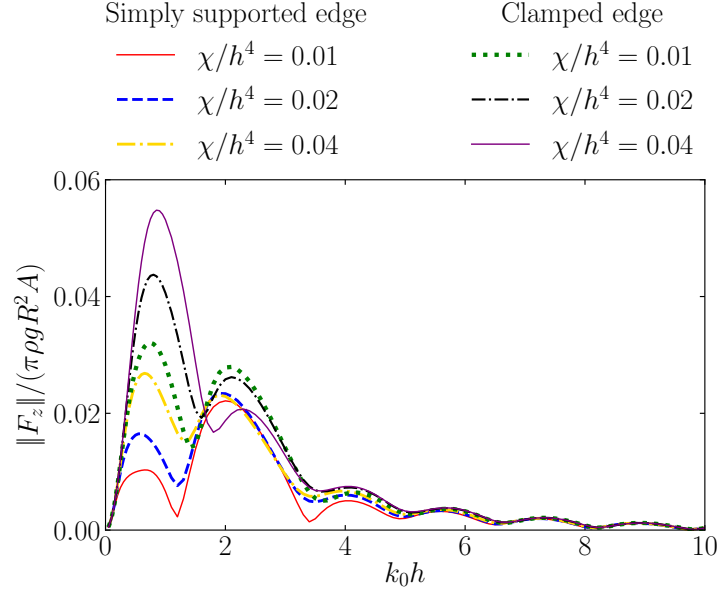
14
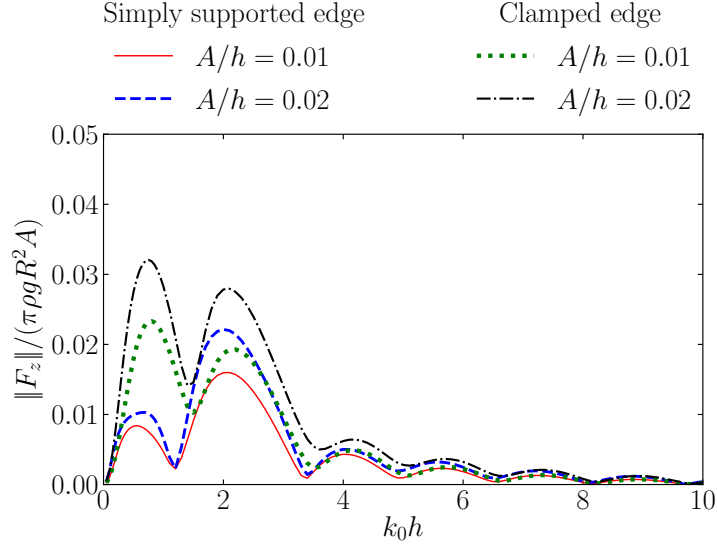
(a) Vertical wave exciting force
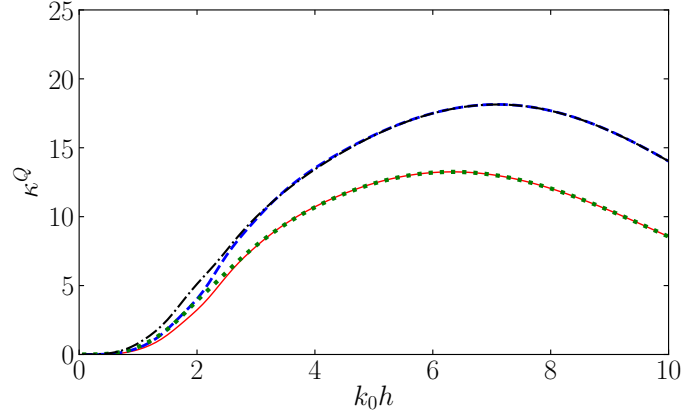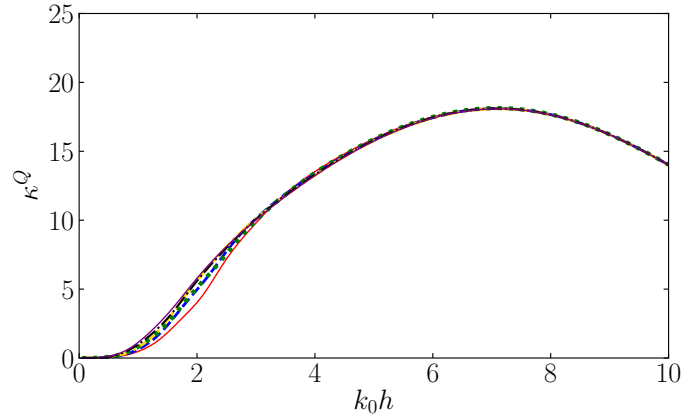

(b) Wave energy absorption

FIG. 6. Normalized wave exciting force $\|F_z\|/(\pi \rho g R^2 A)$ and wave energy absorption κ^Q versus nondimensional wavenumber $k_0 h$ for different wave amplitudes at $R/h = 2.0$, $d/h = 0.2$, $\chi/h^4 = 0.01$, $\gamma/h = 0.01$, $\tau = 0.2$, $\mu = 0.5$ and $\nu = 0.3$.

the nondimensional wave energy absorption κ^Q can reach 25.20 and 26.26 for $A/h = 0.01$ and $A/h = 0.02$, respectively, at $k_0 h \approx 8.4$.

The wave exciting force acting on the disk is displayed in Fig. 9. The parameters are the same as in Fig. 8. When τ is approaching zero, the disk becomes impermeable, and there is a peak in the wave exciting force at $k_0 h \approx 0.7$ for both $A/h = 0.01$ and $A/h = 0.02$. Moreover, the peak value for $A/h = 0.02$ is higher than that for $A/h = 0.01$. With the increasing the open-area ratio τ, the wave exciting force drops dramatically. Therefore, perforating a disk can appreciably reduce the

15

(a) Vertical wave exciting force

(b) Wave power absorption

FIG. 7. Normalized wave exciting force $\|F_z\|/(\pi \rho g R^2 A)$ and wave energy absorption κ^Q versus nondimensional wavenumber $k_0 h$ for different flexural rigidity coefficients at $R/h = 2.0$, $d/h = 0.2$, $A/h = 0.02$, $\gamma/h = 0.01$, $\tau = 0.2$, $\mu = 0.5$ and $\nu = 0.3$.

wave force experienced. This feature has been made use of in the installation of subsea modules to mitigate the environmental loads [20].
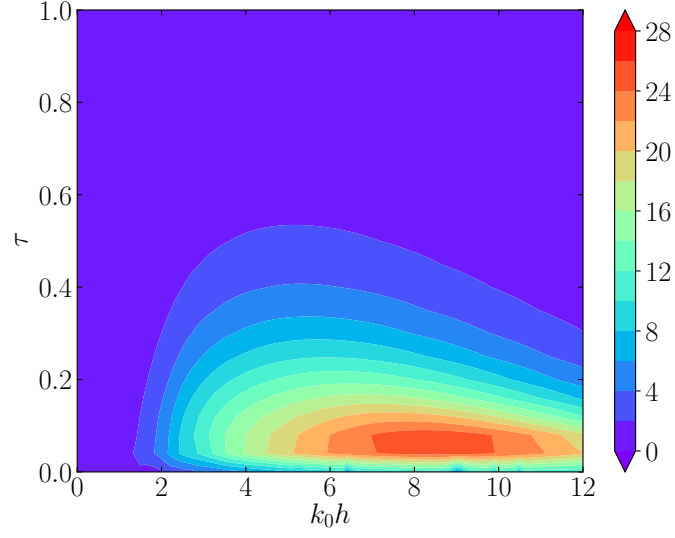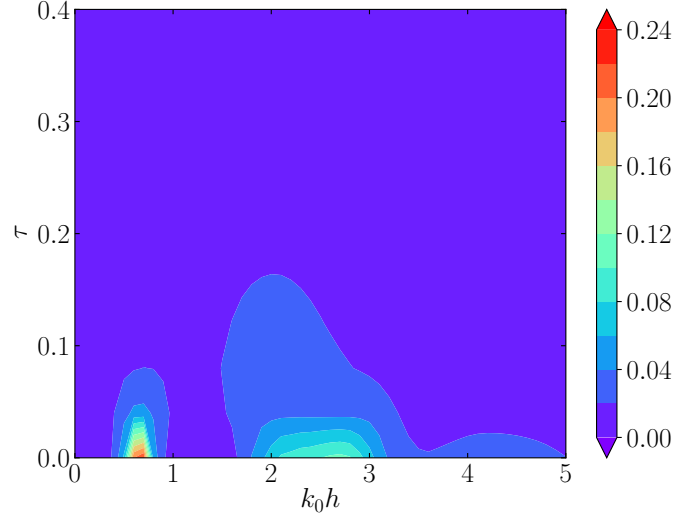
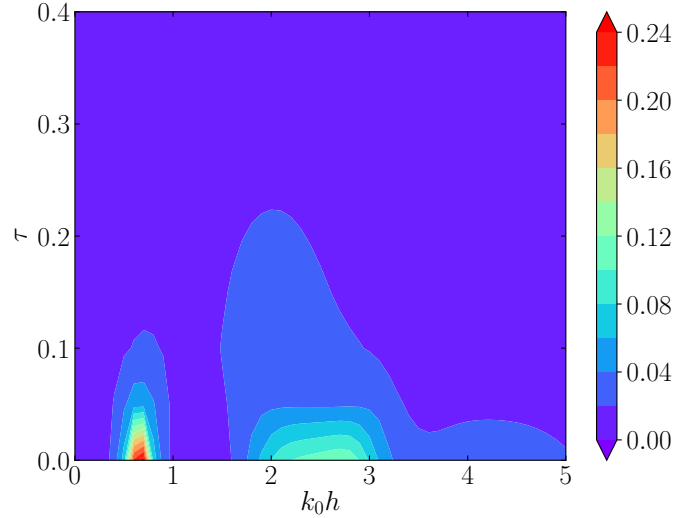(a) $A/h = 0.01$
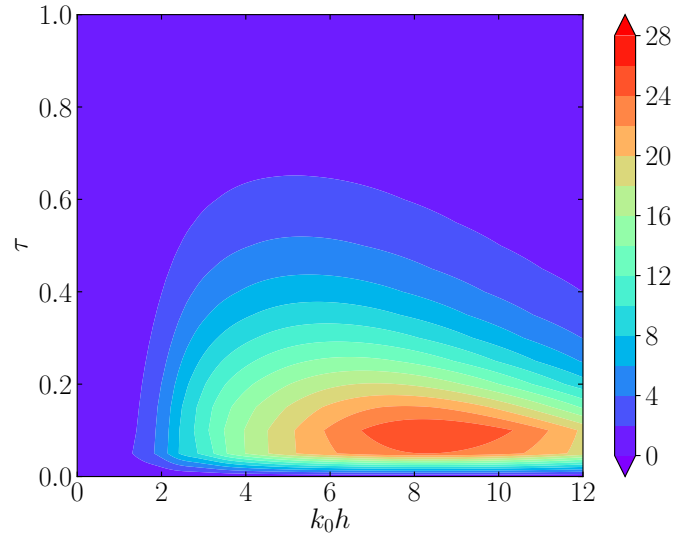
(b) $A/h = 0.02$

FIG. 8. Contour plot of nondimensional wave energy absorption κ^Q by a perforated elastic disk with the edge simply supported varying with nondimensional wavenumber k_0h and open-area ratio τ at $R/h = 2.0$, $d/h = 0.2$, $\gamma/h = 0.01$, $\mu = 0.5$ and $\nu = 0.3$.

D. Comparison with the disk subjected to the linear pressure discharge condition

To investigate the maximum wave energy absorption for different pressure drop conditions, the comparison with the results for the linear pressure drop condition is now made. Figure 10 exhibits the contour plots of nondimensional wave energy absorption κ^L by a perforated flexible

(a) $A/h = 0.01$

(b) $A/h = 0.02$

FIG. 9. Contour plot of normalized wave exciting force $\|F_z\|/(\pi\rho g R^2 A)$ acting on a perforated elastic disk with the edge simply supported varying with nondimensional wavenumber $k_0 h$ and open-area ratio τ at $R/h = 2.0$, $d/h = 0.2$, $\gamma/h = 0.01$, $\mu = 0.5$ and $\nu = 0.3$.

disk subjected to the linear pressure discharge condition. For brevity, the vertical axis is scaled with respect to $b/(1+b)$ ranging from 0 to 1. The maximum wave energy absorbed associated with the linear pressure drop condition is $\kappa^L = 26.28$, which is comparable with the results for the quadratic pressure drop model in Fig. 8. The maximum wave energy occurs at $k_0 h = 8.5$ and $b/(1+b) = 0.8$ corresponding to $b = 4$. To look into the connection with the quadratic model, an

18

empirical formula for linear perforation coefficient given in [37] is introduced

$$b = \frac{(17.8/\varepsilon + 143.2)\tau^2}{1 + 1.06\tau}, \tag{31}$$

where $\varepsilon = k_0 A$ denotes the incident wave slope. For a small wave slope $\varepsilon = 0.03$, $b = 4$ corresponds to an open-area ratio $\tau = 0.077$ which is close to the value 0.08 for the quadratic pressure drop model. At a large wave slope $\varepsilon = 0.3$, however, $b = 4$ corresponds to $\tau = 0.15$ which appreciably deviates from 0.08. Therefore, the incident wave frequency and open-area ratio at which the maximum wave power is harnessed determined by the linear pressure model are almost consistent with ones by the quadratic pressure drop condition at a small wave slope, but inconsistency is witnessed when the wave slope is large. Moreover, the fact that the maximum value of wave power captured is dependent on the wave amplitude cannot be represented by the linear pressure discharge model.
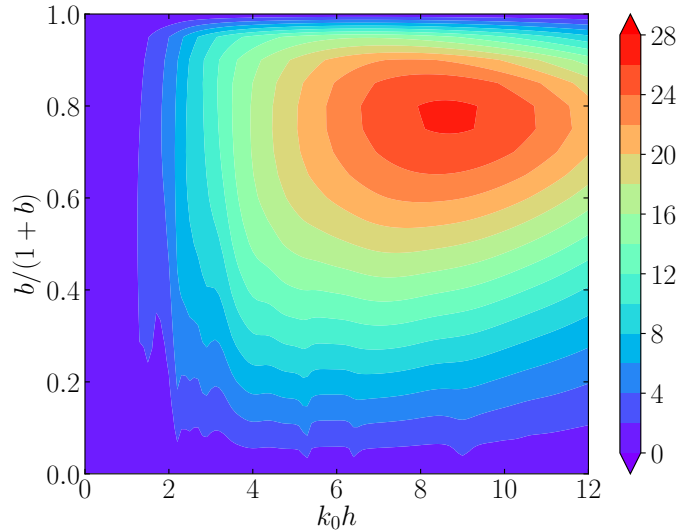

FIG. 10. Contour plot of nondimensional wave energy absorption κ^L by a perforated elastic disk subjected to the linear pressure discharge condition with the edge simply supported varying with nondimensional wavenumber $k_0 h$ and perforation coefficient $b/(1+b)$ at $R/h = 2.0$, $d/h = 0.2$, $\gamma/h = 0.01$ and $\nu = 0.3$.

E. Effect of inclination angle

In the preceding analysis, the disk is horizontally placed. Here we consider scenarios of an inclined disk. The disk is rotated with respect to an axis parallel to Oy axis, and the inclination angle

is defined positive when the upwave side is upward slanting. Figure 11 depicts the wave energy extraction from perforated elastic disks with the edge simply supported at $R/h = 2.0$, $d/h = 0.2$, $A/h = 0.02$, $\chi/h^4 = 0.01$, $\gamma/h = 0.01$, $\tau = 0.08$, $\mu = 0.5$, and $\nu = 0.3$. The incident wave heading angle is $\beta = 0°$, which is in line with positive Ox axis. Besides the horizontal deployment, two slanting deployments for inclination angles $\alpha = \pm 3°$ are also considered. In the range $k_0 h < 7$, the wave wave power extraction for three deployments is commensurate. In the short wave range $k_0 h > 7$, however, a slanting disk, no matter whether upward or downward, harnesses appreciably more wave energy than that by a horizontal disk. Specifically, a disk with the upwave side downward slanting ($\alpha < 0$) can harness even larger wave power.
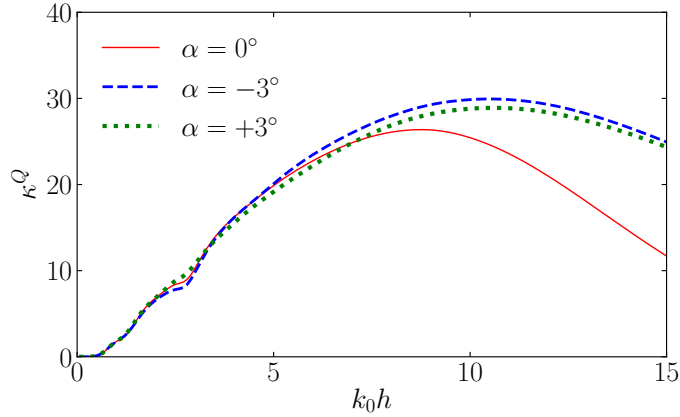

FIG. 11. Wave energy absorption κ^Q by a simply supported perforated elastic disk as a function of nondimensional wavenumber $k_0 h$ for different inclination angles, including: $\alpha = 0°$, $-3°$, and $+3°$, at $R/h = 2.0$, $d/h = 0.2$, $A/h = 0.02$, $\gamma/h = 0.01$, $\tau = 0.08$, $\mu = 0.5$ and $\nu = 0.3$.

F. Hydroelastic deflections of a single disk

Figures 12 and 13 exhibit the normalized hydroelastic deflection $\|\eta\|/A$ of a perforated elastic disk subjected to the clamped and simply supported edge conditions, respectively. The deflection patterns for different wave amplitudes (a): $A/h = 0.01$; (b): $A/h = 0.02$ are displayed in subplots (a) and (b). By comparing subplots (a) and (b), the nondimensional hydroelastic deflection $\|\eta\|/A$ is also dependent on wave amplitude A, and a higher wave amplitude excites larger normalized hydroelastic deflection. As for the displacement of hydroelastic deflections, the hydroelastic deflection subjected to the simply supported edge condition as in Fig. 13 is appreciably larger than

that to the clamped edge as in Fig. 12, whereas there is an opposite tendency in the wave exciting forces as in Fig. 6 (a). Therefore, stronger constraints at the edge can result in a reduction in the hydroelastic deflections but an increase in the wave exciting forces.
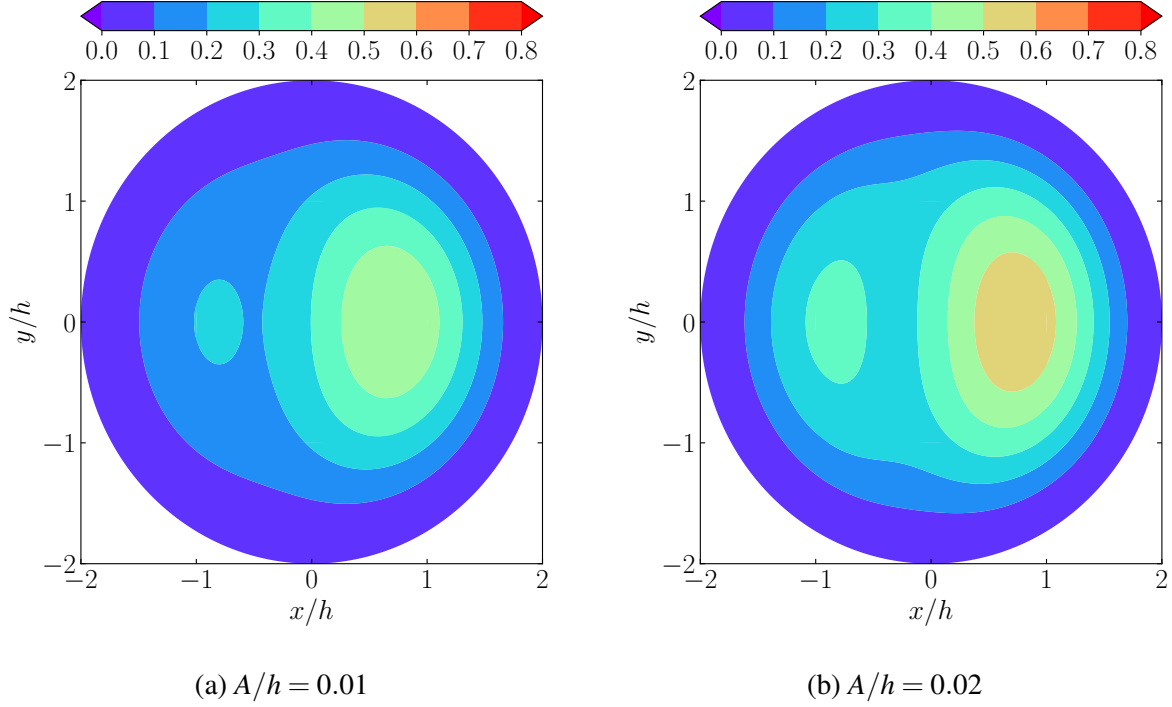

(a) $A/h = 0.01$ (b) $A/h = 0.02$

FIG. 12. Modulus of normalized hydroelastic deflection $\|\eta\|/A$ of a perforated flexible disk subjected to a quadratic pressure discharge condition under a clamped edge condition at $k_0 h = 2.0$, $\beta = 0°$, $R/h = 2.0$, $d/h = 0.2$, $\chi/h^4 = 0.01$, $\gamma/h = 0.01$, $\tau = 0.2$, and $\mu = 0.5$.

G. Hydroelastic deflections of two disks in a side-by-side configuration

Figures 14 and 15 exhibit the normalized hydroelastic deflections of two perforated flexible disks in a side-by-side configuration for clamped edge and simply supported edge conditions, respectively. The centers of two disks are located at $(x_1^c, y_1^c, z_1^c)/h = (0.0, 2.5, -0.2)$ and $(x_2^c, y_2^c, z_2^c)/h = (0.0, -2.5, -0.2)$. The hydroelastic deflection patterns for different wave incidence angles $\beta = 0°$, $\beta = 45°$, and $\beta = 90°$ are displayed in subplots (a), (b), and (c), respectively. As also observed for the single disk scenario, a disk under a clamped edge condition with stronger constraints has smaller hydroelastic deflection than that subjected to a simply supported edge. When the wave incidence direction is in line with the deployment line $\beta = 90°$ as in subplots (c), the lee side disk has much smaller hydroelastic deflection than the weather side one. The reason is
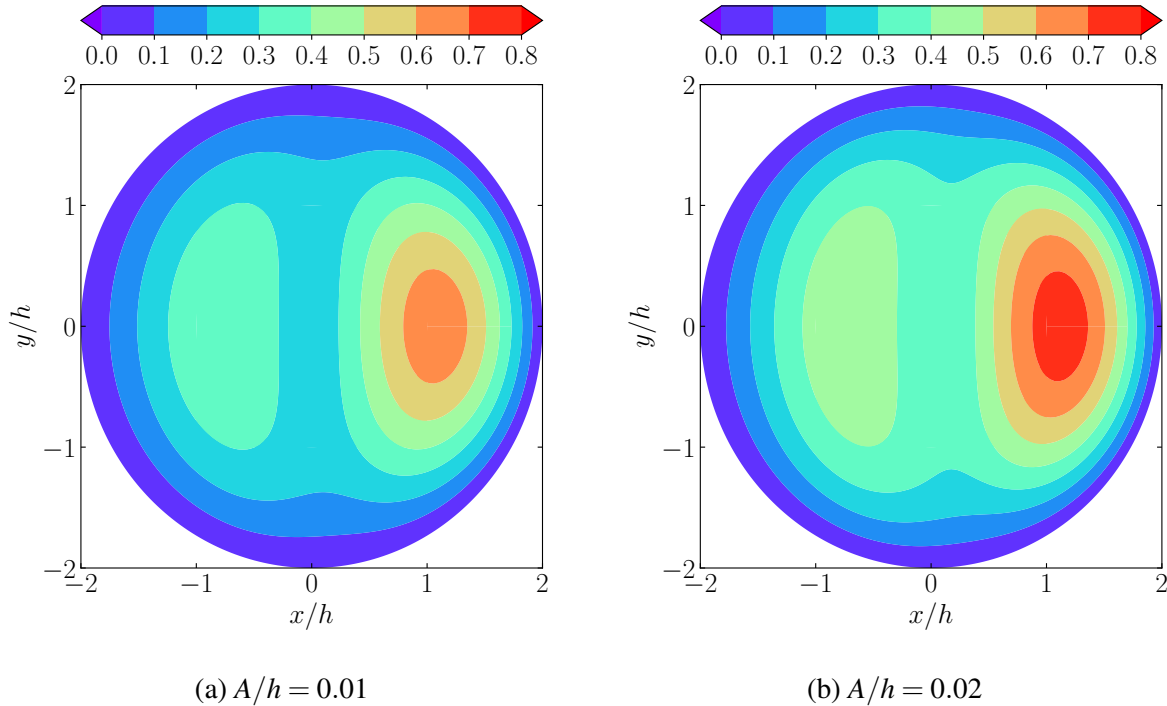
(a) $A/h = 0.01$　　　　　　　　　　　　　(b) $A/h = 0.02$

FIG. 13. Same as Fig. 12 but for simply supported edges with the Poisson's ratio $v = 0.3$.

that the weather side disk acts as a 'breakwater', appreciably dissipating waves downstream. As a consequence, the lee side disk experiences much smaller hydroelastic deformation.

VII.   CONCLUSIONS AND FUTURE PERSPECTIVES

A numerical model is developed via fully coupling the boundary element method for hydrodynamic loads and modal functions for structural deformation to investigate interactions between water waves and perforated elastic disks. The disks are either simply supported or clamped at their edges, the quadratic pressure discharge condition is applied. After verification with benchmark results, a multi-parameter analysis has been carried out to delve into flow physics concerning wave exciting force, hydroelastic deformation, and wave energy extraction. Through this study, the following conclusions are drawn:

1. Nondimensional hydrodynamic responses, including: wave exciting force, wave energy absorption, and hydroelastic deflection, are dependent on the incident wave amplitude because of nonlinear characteristics of the quadratic pressure drop condition. Generally, the higher wave amplitude is, the larger hydrodynamic responses are induced.
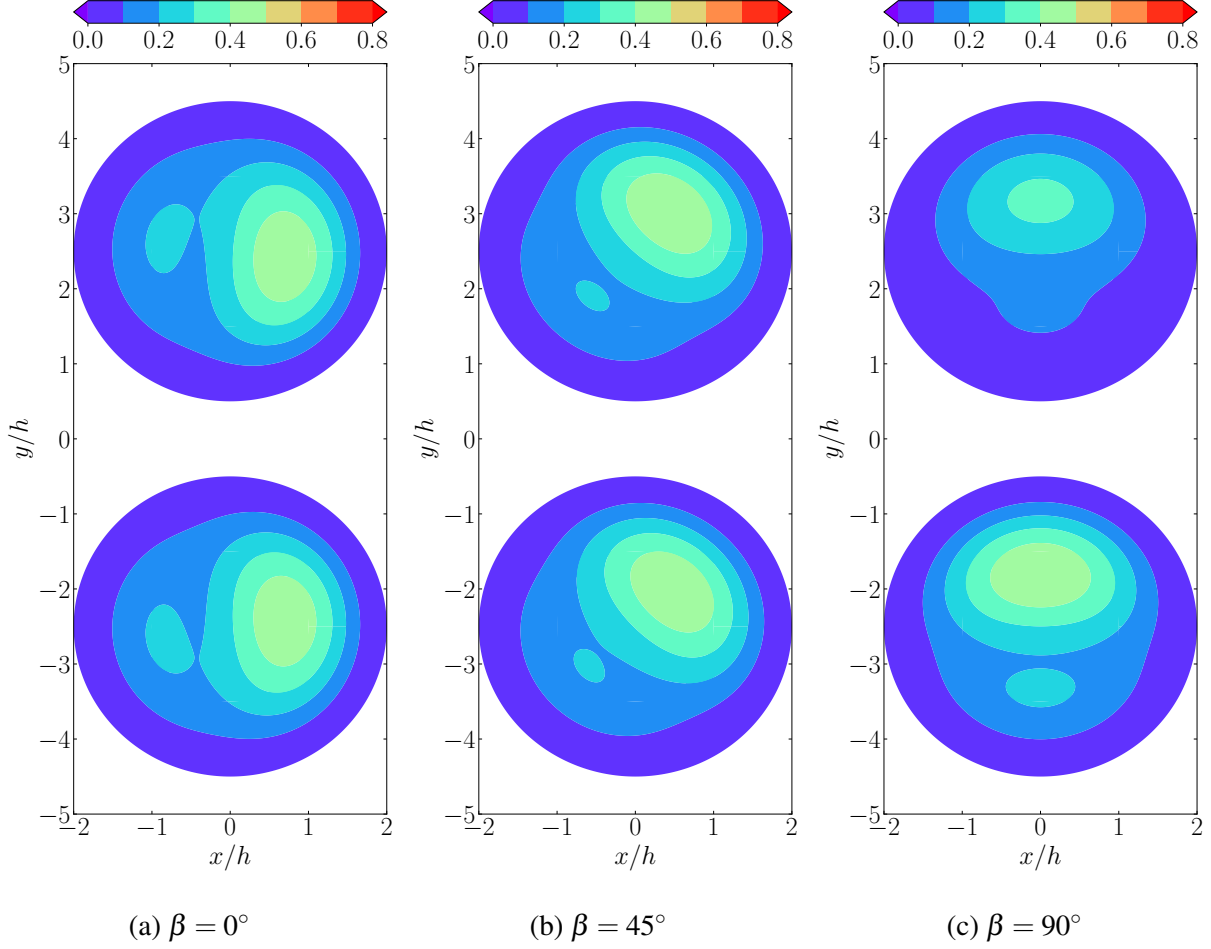
22

FIG. 14. Modulus of normalized hydroelastic deflection of two identical perforated disks $\|\eta\|/A$ with the edge clamped in a side-by-side configuration at $k_0 h = 2.0$, $A/h = 0.01$, $R/h = 2.0$, $d/h = 0.2$, $\chi/h^4 = 0.01$, $\gamma/h = 0.01$, $\tau = 0.2$, and $\mu = 0.5$. Two disks have the same immersion depths, and the center-to-center distance is $l/h = 5.0$.

2. Increasing the flexural rigidity of the disk or rendering stronger constraints at the edge leads to an increase in the wave exciting forces and a reduction in hydroelastic deformation. Nevertheless, in the computed range of wave frequencies, they have negligible effects on wave energy absorption.

3. It is possible to devise an optimal open-area ratio so that high wave power is harnessed. The optimal open-area ratio for the quadratic pressure drop model is only consistent with the one for the linear pressure drop model at a small wave steepness, and appreciable inconsistency is observed at a large wave slope. Moreover, the linear pressure discharge model cannot capture the dependency of the maximum wave power captured on the wave amplitude, indi-

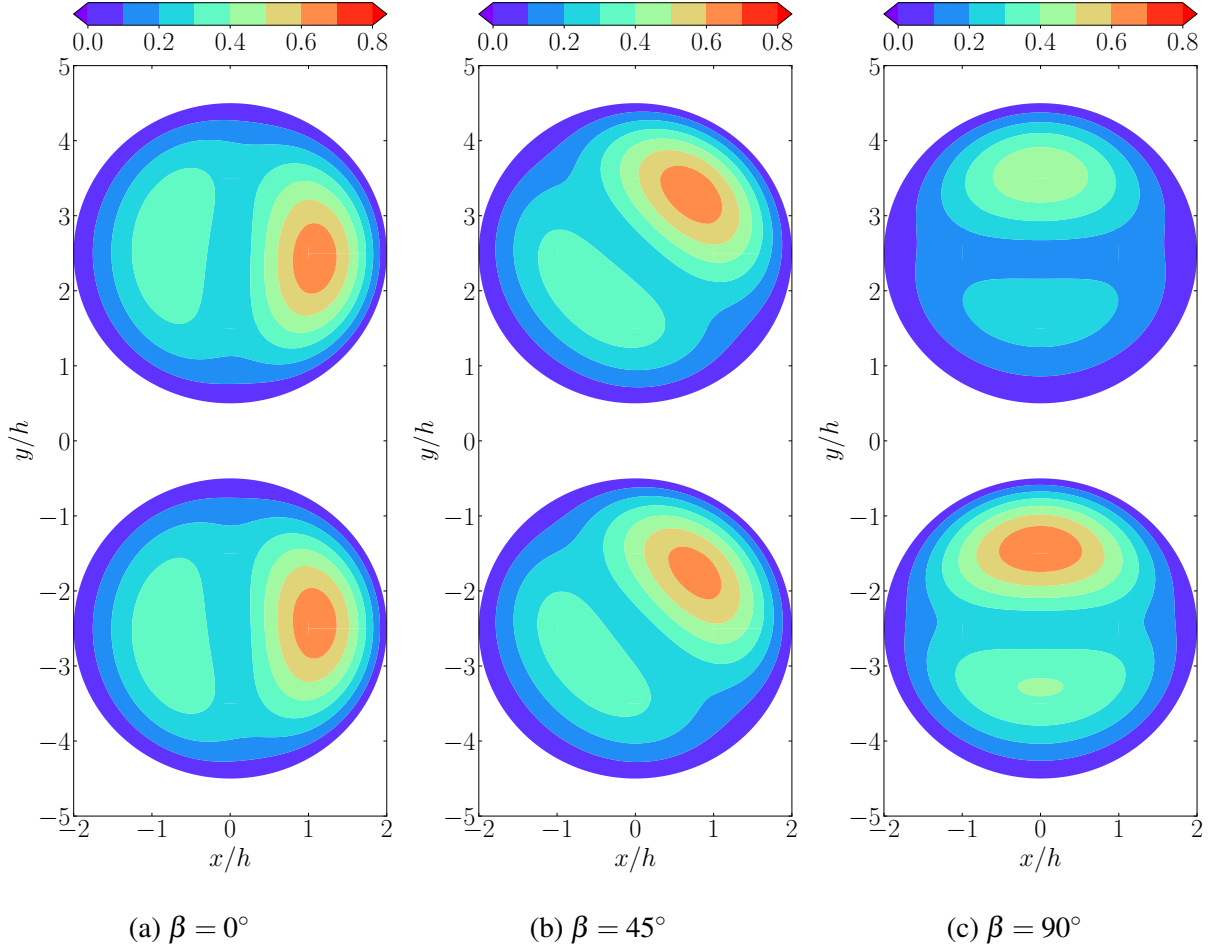(a) $\beta = 0°$ (b) $\beta = 45°$ (c) $\beta = 90°$

FIG. 15. Same as Fig. 14 but for simply supported edges with the Poisson's ratio $\nu = 0.3$.

cating the limitation of the linear pressure drop model.

4. A disk with the upwave side downward slanting can harness more energy than that by a horizontal counterpart especially in short waves. This feature can be used either in a wave basin to mitigate wave reflection or in plate-shaped wave energy converters to capture higher energy.

5. When the incident waves propagate in line with the deployment line of multiple disks, the lee side disk has much smaller responses because waves are considerably attenuated by the weather side disk.

In view of the fact that flexible bodies can extend the theoretical limit of wave power absorption [38], the present model will be generalized to study flexible plate shaped wave energy converters with discrete power take-off (PTO) system as in [39]. Moreover, a perforated plate subjected to the

quadratic pressure drop condition can also be applied as a fictitious dissipation surface to model the energy dissipation due to flow separation [40–42]. In view of small thickness of disks, viscous effects may play a part, and the energy dissipation due to flow separation from the edge will be considered in future studies.

ACKNOWLEDGMENT

[1] B. Molin, "On the added mass and damping of periodic arrays of fully or partially porous disks," Journal of Fluids and Structures **15**, 275–290 (2001).

[2] L. Tao, Y.-M. Molin, B.and Scolan, and K. Thiagarajan, "Spacing effects on hydrodynamics of heave plates on offshore structures," Journal of Fluids and Structures **23**, 1119–1136 (2007).

[3] M. H. Meylan, L. G. Bennetts, and M. A. Peter, "Water-wave scattering and energy dissipation by a floating porous elastic plate in three dimensions," Wave Motion **70**, 240–250 (2017).

[4] S. Zheng, M. H. Meylan, D. Greaves, and G. Iglesias, "Water-wave interaction with submerged porous elastic disks," Physics of Fluids **32**, 047106 (2020).

[5] S. Zheng, M. H. Meylan, G. Zhu, D. Greaves, and G. Iglesias, "Hydroelastic interaction between water waves and an array of circular floating porous elastic plates," Journal of Fluid Mechanics **900** (2020).

[6] H. Liang, S. Zheng, Y. Shao, K. H. Chua, Y. S. Choo, and D. Greaves, "Water wave scattering by impermeable and perforated plates," Physics of Fluids **33**, 077111 (2021).

[7] B. Molin and J. M. Fourest, "Numerical modeling of progressive wave absorbers," in *Proceeding of the 7th International Workshop on Water Waves and Floating Bodies, Val de Reuil, France* (1992) pp. 199–203.

[8] I. H. Cho and M. H. Kim, "Interactions of a horizontal flexible membrane with oblique incident waves," Journal of Fluid Mechanics **367**, 139–161 (1998).

[9] I. H. Cho and M. H. Kim, "Wave absorbing system using inclined perforated plates," Journal of Fluid Mechanics **608**, 1–20 (2008).

[10] Y. Liu, Y. Li, B. Teng, J. Jiang, and B. Ma, "Total horizontal and vertical forces of irregular waves on partially perforated caisson breakwaters," Coastal Engineering **55**, 537–552 (2008).

[11] H. Behera and T. Sahoo, "Hydroelastic analysis of gravity wave interaction with submerged horizontal flexible porous plate," Journal of Fluids and Structures **54**, 643–660 (2015).

[12] Y. Liu and H.-J. Li, "Iterative multi-domain BEM solution for water wave reflection by perforated caisson breakwaters," Engineering Analysis with Boundary Elements **77**, 70–80 (2017).

[13] C. C. Mei, M. Stiassnie, and D. K. P. Yue, *Theory and applications of ocean surface waves (3rd edition)* (World Scientific, 2017).

[14] A. T. Chwang, "A porous-wavemaker theory," Journal of Fluid Mechanics **132**, 395–406 (1983).

[15] A. T. Chwang and A. T. Chan, "Interaction between porous media and wave motion," Annual Review of Fluid Mechanics **30**, 53–84 (1998).

[16] X. Yu and A. T. Chwang, "Wave motion through porous structures," Journal of Engineering Mechanics **120**, 989–1008 (1994).

[17] Y. Liu and Y.-C. Li, "An alternative analytical solution for water-wave motion over a submerged horizontal porous plate," Journal of Engineering Mathematics **69**, 385–400 (2011).

[18] S. A. Selvan, H. Behera, and T. Sahoo, "Reduction of hydroelastic response of a flexible floating structure by an annular flexible permeable membrane," Journal of Engineering Mathematics **118**, 73–99 (2019).

[19] G. I. Taylor, "Fluid flow in regions bounded by porous surfaces," Proceedings of the Royal Society of London. Series A. Mathematical and Physical Sciences **234**, 456–475 (1956).

[20] B. Molin, "Hydrodynamic modeling of perforated structures," Applied Ocean Research **33**, 1–11 (2011).

[21] O. M. Faltinsen, R. Firoozkoohi, and A. N. Timokha, "Steady-state liquid sloshing in a rectangular tank with a slat-type screen in the middle: Quasilinear modal analysis and experiments," Physics of Fluids **23**, 042101 (2011).

[22] S. Crowley and R. Porter, "The effect of slatted screens on waves," Journal of Engineering Mathematics **76**, 33–57 (2012).

[23] E. B. L. Mackay, H. Liang, and L. Johanning, "A BEM model for wave forces on structures with thin porous elements," Journal of Fluids and Structures **102**, 103246 (2021).

[24] W. W. Jamieson and E. P. Mansard, "An efficent upright wave absorber," in *ASCE Specialty Conference on Coastal Hydrodynamics, University of Delaware, USA* (1987) pp. 124–139.

[25] S. An and O. M. Faltinsen, "An experimental and numerical study of heave added mass and damping of horizontally submerged and perforated rectangular plates," Journal of Fluids and Structures **39**, 87–101 (2013).

[26] E. B. L. Mackay, W. Shi, D. Qiao, R. Gabl, T. Davey, D. Ning, and L. Johanning, "Numerical and experimental modelling of wave interaction with fixed and floating porous cylinders," Ocean Engineering **242**, 110118 (2021).

[27] A. Korobkin, E. I. Părău, and J.-M. Vanden-Broeck, "The mathematical challenges and modelling of hydroelasticity," Philosophical Transactions of the Royal Society A: Mathematical, Physical and Engineering Sciences **369**, 2803–2812 (2011).

[28] J. N. Newman, *Marine Hydrodynamics* (Massachusetts Institute of Technology Press, 1977).

[29] B. Molin, *Hydrodynamique des Structures Offshore* (Editions Technip, 2002).

[30] N. F. Parsons and P. A. Martin, "Scattering of water waves by submerged plates using hypersingular integral equations," Applied Ocean Research **14**, 313–321 (1992).

[31] P. A. Martin and L. Farina, "Radiation of water waves by a heaving submerged horizontal disc," Journal of Fluid Mechanics **337**, 365–379 (1997).

[32] J. V. Wehausen and E. V. Laitone, "Surface waves," Hanbuch der Physik **9**, 446–778 (1960).

[33] M. Abramowitz and I. A. Stegun, *Handbook of Mathematical Functions: with Formulas, Graphs, and Mathematical Tables*, 55 (National Bureau of Standards, 1964).

[34] H. Liang, Y. Shao, and J. Chen, "Higher-order derivatives of the Green function in hyper-singular integral equations," European Journal of Mechanics - B/Fluids **86**, 223–230 (2021).

[35] C. M. Linton and P. McIver, *Handbook of mathematical techniques for wave/structure interactions* (Chapman and Hall/CRC, 2001).

[36] B. Molin, F. Remy, and T. Rippol, "Experimental study of the heave added mass and damping of solid and perforated disks close to the free surface," in *Proceedings of the 12th International Congress of the International Maritime Association of the Mediterranean (IMAM 2007), Varna, Bulgaria* (2007) pp. 879–887.

[37] F. Zhao, W. Bao, T. Kinoshita, and H. Itakura, "Theoretical and experimental study on a porous cylinder floating in waves," Journal of Offshore Mechanics and Arctic Engineering **133**, 011301 (2011).

[38] R. Porter, S. Zheng, and D. Greaves, "Extending limits for wave power absorption by axisymmetric devices," Journal of Fluid Mechanics **924**, A39 (2021).

[39] S. Michele, S. Zheng, and D. Greaves, "Wave energy extraction from a floating flexible circular plate," Ocean Engineering (2022).

[40] O. M. Faltinsen and A. N. Timokha, "On damping of two-dimensional piston-mode sloshing in a rectangular moonpool under forced heave motions," Journal of Fluid Mechanics **772**, 1–11 (2015).

[41] L. Tan, L. Lu, G.-Q. Tang, L. Cheng, and X.-B. Chen, "A viscous damping model for piston mode resonance," Journal of Fluid Mechanics **871**, 510–533 (2019).

[42] H. Liang, K. H. Chua, H. C. Wang, and Y. S. Choo, "Numerical and experimental investigations into fluid resonance in a gap between two side-by-side vessels," Applied Ocean Research **111**, 102581 (2021).